Ultramicroscopy 276 (2025) 114167

Contents lists available at ScienceDirect

Ultramicroscopy

journal homepage: www.elsevier.com/locate/ultramic

Multimode objective lens for momentum microscopy and XPEEM: Theory

Olena Tkach *, Gerd Schönhense

Johannes Gutenberg-Universität, Institut für Physik, 55128, Mainz, Germany

ARTICLE INFO

Keywords:
Momentum microscopy
PEEM
XPEEM
Cathode lens
Space charge
Aberrations

ABSTRACT

The strong electric field between the sample and the extractor is at the heart of cathode lenses and a crucial factor for high resolution. However, fields in the range of 3-10 kV/mm can be a source of complications. Local field enhancement at sharp edges or microscopic protrusions of cleaved samples can lead to field emission or flashovers. In addition, slow background electrons drawn into the microscope column contribute to space charge effects. A novel objective configuration, optimized by ray-tracing simulations at energies from a few eV to 6 keV, significantly reduces the field at the sample. One or more annular electrodes concentric to the extractor can shape the electric field in front of the sample. The formation of a 'gaplens' reduces the field to values below the 1 kV/mm range. Tuning the field to zero is advantageous for 3D structured samples. Retarding fields repel slow electrons, suppressing space charge effects. The properties of the different lens modes are investigated using ray tracing and determination of aberration coefficients. Despite its much lower electric field, the gaplens mode exhibits smaller aberrations and enables larger fields of view for both momentum and real space imaging. At electric fields as low as 1200 and 880 V/mm, the accessible solid angle interval in the gaplens mode is three times larger than in the extractor mode (with a start energy of 100 eV and a *k*-resolution of 10^{-2} Å^{-1}). Due to the elimination of space charge effects in the retarding field mode, XPEEM resolutions in the range of 25 nm are predicted. The ray tracing results are confirmed by the spherical and chromatic aberration coefficients of the real-space and *k*-space images.

1. Introduction

The performance of cathode lens microscopes such as photoemission electron microscopes (PEEMs), low-energy electron microscopes (LEEMs) and momentum microscopes (MMs) depends on the strength of the accelerating field between the sample and the extractor. The simplified treatment by Brüche and Recknagel [1,2] was subsequently refined by extensive theoretical work by Bauer and Rempfer et al. [3,4]. Finally, Tromp et al. derived the aberration coefficients of cathode lenses up to the fifth order [5,6]. Typical cathode lenses of PEEMs and MMs are designed for extractor fields in the range of 3-10 kV/mm. Such fields can be problematic for cleaved samples, which often have sharp corners or protruding lamellae, with the potential for field emission or even flashovers.

A second problem can arise from the space charge interaction. The extractor field attracts slow electrons into the lens column, where they exert Coulomb forces on the photoelectrons. The number of slow secondary electrons, resulting from cascade scattering processes, can potentially exceed the number of true photoelectrons by several orders of magnitude. This is particularly problematic in experiments using pulsed X-ray beams from synchrotrons or free-electron lasers. The space-charge effect has been observed to impose a resolution limit in X-ray excited PEEM (XPEEM) [7–9] and to induce a Lorentzian deformation of the iso-energetic planes in MMs [10]. In time-resolved experiments using the pump-probe technique, another species of slow electrons can be released by the pump pulse via multiphoton photoemission (nPPE) transitions. The long-range Coulomb interaction between this species and the photoelectrons leads to artifact signals that can obscure the true effects [11].

The extractor field has thus been identified as a potential source of complications in several cases. The prevailing notion that strong extractor fields are essential for optimal cathode lens function limits the use of this technique because of the practical constraints that impede its application. This prompted us to investigate alternative front lens configurations with the goal of bypassing the strong extractor field.

In the novel lens configuration, the homogeneous accelerating field is replaced by a *gaplens*, which is an additional lens located in the space between the sample and the first electrodes. The potential distribution is

* Corresponding author.
E-mail address: tkachole@uni-mainz.de (O. Tkach).

https://doi.org/10.1016/j.ultramic.2025.114167
Received 13 September 2024; Received in revised form 8 May 2025; Accepted 16 May 2025
Available online 23 May 2025

formed by one or two ring electrodes that are concentric with the extractor. The ring electrodes do not obstruct the space between the sample and the extractor, but can generate a variety of lens fields within the gap. By applying different voltages, the field at the sample surface can be tuned from a strongly accelerating to a retarding configuration. Each has a different effect on the imaging behavior.

This work investigates the different operating modes of the gaplens geometry through ray tracing simulations. Despite the reduced field at the sample, which avoids the risk of field emission, spherical and chromatic aberration in the *k*-image in the back focal plane are significantly reduced compared to the extractor mode. This enables much larger *k*-fields of view with up to 18 $Å^{-1}$ in diameter, which is advantageous for photoelectron diffraction studies. In XPEEM mode fields of view larger than 4 mm are a crucial aspect for the upcoming full-field imaging PAXRIXS technique [12]. Reducing the electric field at the sample is advantageous for samples with corrugations or electrodes on the surface. Retarding fields repel slow electrons and eliminate most of the vacuum space-charge interaction in time-resolved pump-probe experiments. The ray tracing results are presented and discussed here. The first experimental results presented in Ref. [13].

2. Multimode front lens

2.1. Motivation and operating principles of the multimode lens

PEEMs and MMs are optimized for different purposes. The goal of PEEMs is high-resolution real-space imaging, while MMs are designed for *k*-space imaging. Depending on the specific application, the quality criteria for MM images may vary. When recording valence band patterns, the quantity of interest is the *k*-resolution. Benchmark values in the range of 0.004 $Å^{-1}$, obtained with a double-hemispherical MM [14] are comparable to those obtained with conventional angle-resolved photoelectron spectroscopy (ARPES) using a hemispherical analyzer (HSA) [15]. For time-of-flight (ToF) MM at higher energies in the soft or hard X-ray range [16,17] additional criteria become relevant. In the context of X-ray photoelectron diffraction (XPD), the size of the observed *k*-field is of paramount importance as it determines the information content of the diffraction patterns. The detection of *k*-fields with diameters larger than 12 $Å^{-1}$ has been demonstrated using hard X-ray excitation [18,19]. For such large *k*-fields, the *spherical aberration* of the lens system is the limiting factor.

With regard to *chromatic aberration*, the circumstances depend on the specific instrument. In the case of HSA-based MMs recording 2D (k_x,k_y) patterns, the bandwidth of the detected electrons is narrow. In experiments with He-lamps, the final energy resolutions achieved with different setups ranged from 4 to 13 meV [20–22]. In synchrotron experiments, the resolution is limited by the bandwidth of the photon beam, typically 30-50 meV in the soft X-ray region and an order of magnitude larger in the hard X-ray range. Under these conditions, chromatic aberration is negligible. ToF-MMs [16,17] simultaneously record 3D (k_x,k_y,E_{kin}) arrays with specific E_{kin} bands. For core-level XPD imaging, the energy band is typically around 500 meV. In this case, the effect of chromatic aberration is small. Chromatic aberration is significant for ToF-MM based ARPES, where bands of several eV width are recorded. The main effect can be eliminated by numerical data treatment [23] (see section 2.2). We note that the aberrations of the objective lens can be compensated by a mirror corrector, which requires an arrangement with two magnetic beam separators [24].

The development of the multimode lens was driven by the aforementioned problems caused by the high field strength (voltage breakthrough) and space charge effects (energy shifts and broadening, image blur). The basic concept behind the design of the new front lens was the ability to vary the field strength at the sample over a wide range, from acceleration to deceleration, by changing the potentials of the extractor and ring electrodes. The primary goal was to optimize the *k*-image quality with an accelerating field of significantly reduced strength compared to classical cathode lenses. For specimens with critical features such as sharp corners or protrusions, this mode should be superior to the extractor mode. The second goal was to develop a retarding mode that would eliminate the main contribution of the space charge effect, especially in pump-probe photoemission experiments at high harmonic generation (HHG) based sources and free-electron lasers (FELs). A systematic ray tracing approach was used to investigate the properties of all modes over a range of lens geometries and kinetic energies. All simulations were performed with the SIMION code [25].

Fig. 1(a-e) show the front part of the novel lens, equipped with two ring electrodes designated R1 and R2. The effect of these electrodes is illustrated by five characteristic lens field distributions. First examples of such electrodes were presented in Ref. [26]. By varying the potentials of R1 and R2, additional degrees of freedom for field shaping can be introduced.

When Ex, R1 and R2 are set to a high positive potential with respect to the sample (here all at 20 kV), the configuration represents the *extractor mode*, Fig. 1(a). The uniform field is $F = U_{Ex}/l$, in this case $F =$ +3.3 kV/mm for a gap between Sa and Ex of l = 6 mm. By reducing the potentials of R1 and R2, an additional converging lens is introduced into the gap. Fig. 1(b) shows the equipotential contours for U_{Ex}= 12 kV and $U_{R1} = U_{R2} = 0$. In this *gaplens mode,* the accelerating field at the sample is significantly reduced, here to +1 kV/mm. By setting R1 and R2 to negative voltages, it is possible to compensate the field at the sample surface. This results in the *zero-field mode* shown in Fig. 1(c), for $U_{Ex} = 8$ kV and $U_{R1} = U_{R2} =$ -10 kV.

A further increase of the negative potentials at the ring electrodes results in the *repeller mode*, as shown in Fig. 1(d), with $U_{R1} = U_{R2} =$ -12 kV. The repelling field is indicated by red equipotential contours, here with a field strength at the sample of -310 V/mm. The saddle point at a potential of $U_S =$ -375 V acts as a high-pass filter, allowing only electrons with initial kinetic energies $E_0 > 375$ eV to pass. The repulsion of a large amount of electrons results in significant reduction of the Coulomb interaction within the beam. Another degree of freedom in field shaping is introduced by setting R1 and R2 to different potentials. It is possible to modify the repelling field in order to create different shapes, and the position of the saddle point can also be adjusted. In the illustrative example shown in Fig. 1(e), where U_{R1} is set to -9.6 kV and U_{R2} is set to +8 kV, the retarding field is reduced, the saddle point is moved closer to the sample, and the refractive power of the gaplens is increased.

Fig. 1(f) shows the geometry of a low-energy prototype of the complete front lens consisting of sample (Sa), extractor (Ex), here one ring element (R), focus (Foc), contrast aperture array (CA) in the reciprocal image plane (dotted red line), and the 1st octupole stigmator (Stig.1), not shown in detail. The gap is l = 6 mm and the extractor hole diameter is 4 mm. Fig. 1(g) shows the second lens group forming the 1st Gaussian image in the plane of the field aperture (FA). The equipotential contours and rays in (f,g) correspond to the gaplens mode and $E_0 = 100$ eV, as will be further illustrated in Fig. 2. The blue rays started from the sample at 100 µm off-center and are imaged in the FA plane at a magnification of 12. The third group of lenses (not shown) is a zoom lens that forms the final *k*-image on the image detector behind the ToF section. Figs. 1(h) and (i) show the front view and cross-section of a prototype of extractor and ring electrode that are used for initial experiments at low kinetic energies.

2.2. Spherical and chromatic aberration in extractor and gaplens modes

A major goal of the present study was to investigate the performance of the *gaplens mode* (Figs. 1(b,f)), which is used to reduce the field at the sample surface. In particular, we addressed the question of how the imaging quality of the gaplens mode compares to that of the extractor mode. The simulations, together with the first experimental validations, were performed for a single ring electrode (R) configuration, like shown in Fig. 1(f). Figs. 2 and 3 provide an answer to this question. Ray tracing simulations were performed for three different initial energies: $E_0 = 100$

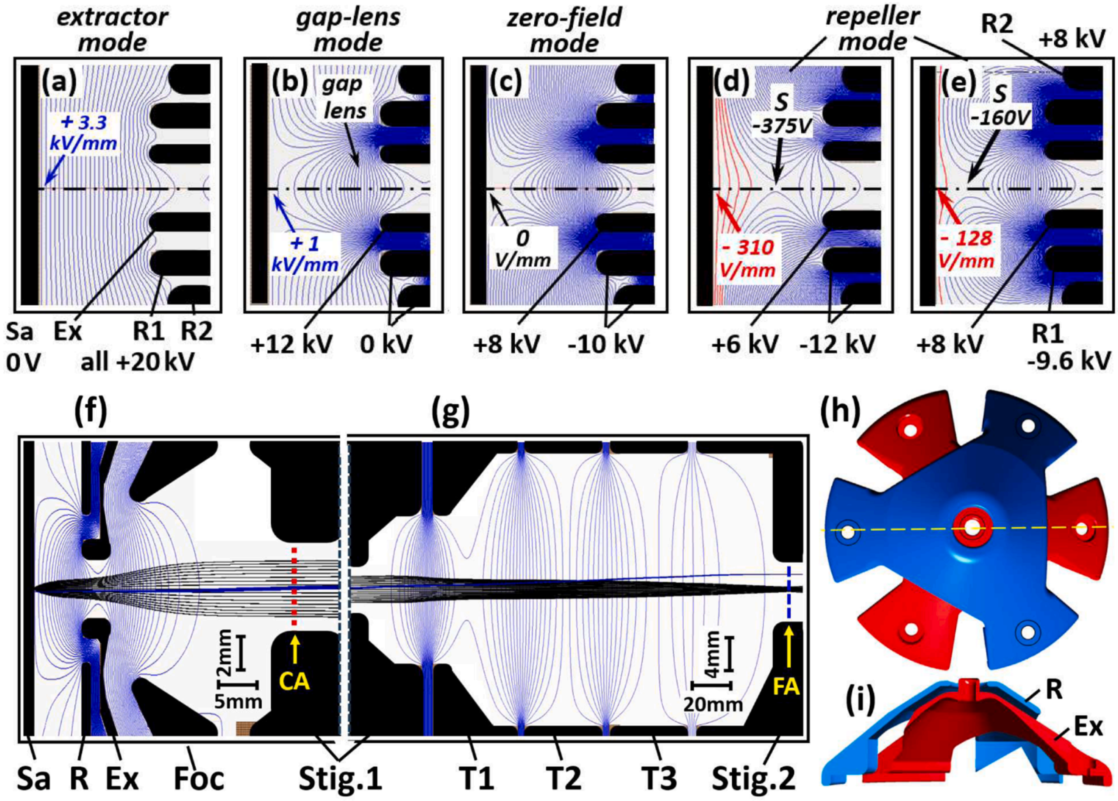

Fig. 1. Operating schemes for the different modes of the multimode front lens, showing the equipotential contours. (a) Classic *extractor mode* with the extractor Ex and ring electrodes R1 and R2 at 20 kV, resulting in a homogeneous field of F= +3.3 kV/mm. (b) *Gaplens mode* with U_{Ex}= 12 kV and U_{R1}= U_{R2} = 0 V, resulting in the formation of an additional lens in front of Ex, which reduces the field at the sample Sa to +1 kV/mm. (c) *Zero-field mode* (F= 0), obtained with U_{Ex} = 8 kV and negative ring electrodes (U_{R1}= U_{R2}= -10 kV). (d) *Repeller mode*, here with F= -310 V/mm, obtained with U_{Ex}= 6 kV and U_{R1}= U_{R2}= -12 kV. The saddle point at U_{S} = -375 V defines the low energy cutoff. (e) *Repeller mode*, modified by setting U_{Ex}= U_{R2}= +8 kV and U_{R1}= -9.6 kV. In (d,e) the retarding field is indicated by red potential contours. (f) Geometry of the complete front lens including the focus electrode (Foc) and the lens element with stigmator 1 and contrast aperture (CA); the dotted red line indicates the 1st k-image. (g) Second lens group, consisting of the transfer lenses T1-T3 and the lens element with stigmator 2 and field aperture (FA). The dashed blue line indicates the 1st Gaussian image. Note the different scale bars in (f,g). (h,i) Top view and cross section of a first prototype of the electrodes Ex and R.

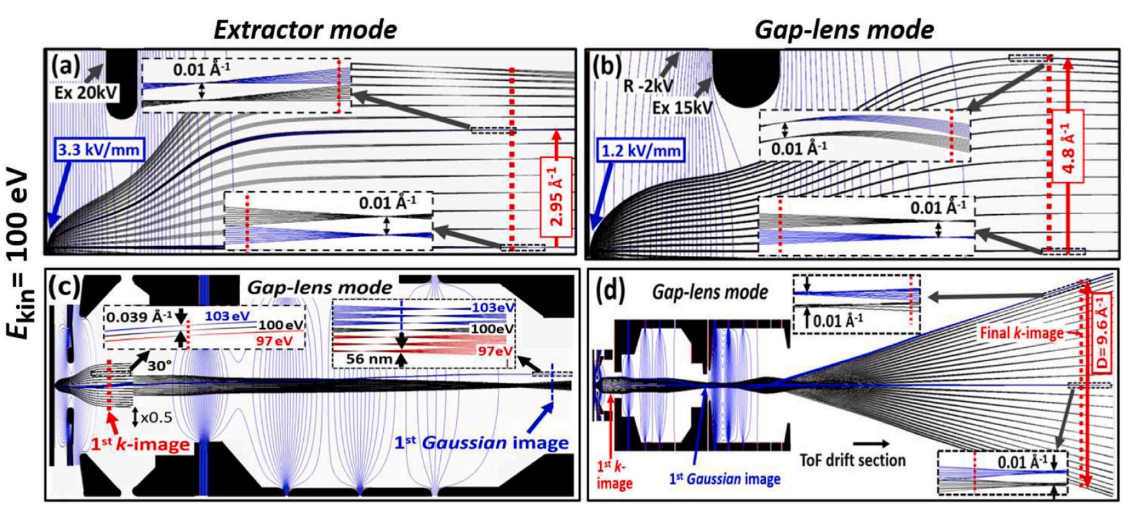

Fig. 2. Comparison of *extractor* and *gaplens modes* for E_0 = 100 eV; source spot diameter 30 µm. Simulations for α_0 = 0-70°, corresponding to a k-field of 9.6 Å^{-1} in diameter. (a) *Extractor mode* with U_{Ex} = U_{R} = 20 kV giving an electric field of F = 3.3 kV/mm. A k-resolution of Δk = 10^{-2} Å^{-1} is obtained for α_0 up to about 35°. The blue and black ray bundles (difference 10^{-2} Å^{-1}) are just separated at 0° (lower inset) and 35° (upper inset); the dotted red lines mark the k-image plane. (b) The same for the *gaplens mode*. Here, a resolution of 10^{-2} Å^{-1} is achieved for α_0 up to 70°. (c) Quantification of the chromatic aberration. The k-image (left inset) shows a significant change in magnification with energy between 97 and 103 eV. The double arrow labeled x0.5 indicates a change in the radial scale. The Gaussian image (right inset) shows both the magnification change and a significant image plane shift. The dashed blue line indicates the Gaussian image plane. (d) Simulation for the whole microscope in gaplens mode. The resolution of Δk = 10^{-2} Å^{-1} is maintained in the final k-image.

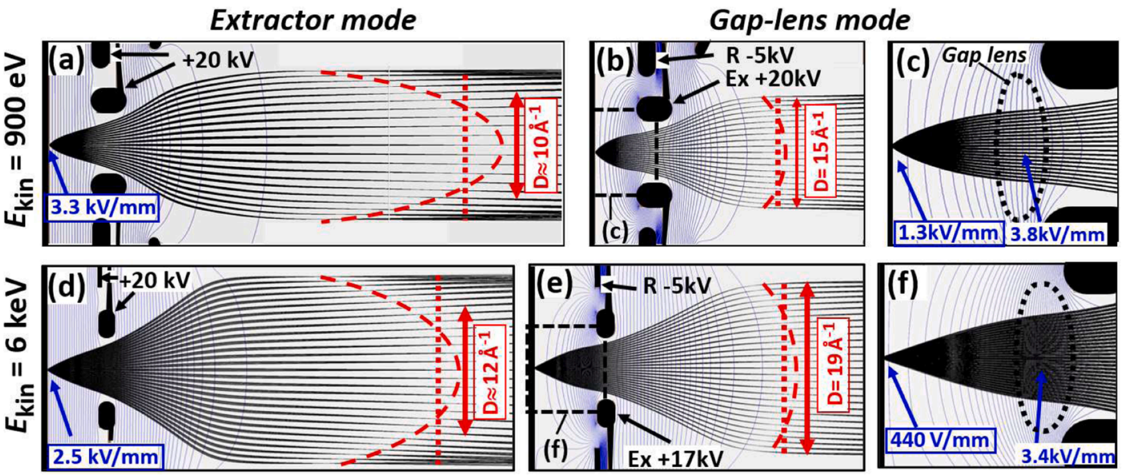

Fig. 3. Comparison of *extractor* and *gaplens modes* for $E_0 = 900$ eV and 6 kV; source spot diameter 100 µm. (a-c) Simulation for α_0 = 0-30°, corresponding to a *k*-field of 15 Å^{-1} in diameter. (a) *Extractor mode* with $U_{Ex} = U_R = 20$ kV giving a *k*-resolution of $\Delta k = 0.015$ Å^{-1} for angles up to $\alpha_0 = 20°$ (dia. 10 Å^{-1}). (b,c) *Gaplens mode* with $U_{Ex} = 20$ kV and U_R = -5 kV (*F*= 1.3 kV/mm). Here $\Delta k = 0.015$ Å^{-1} is obtained for angles up to $\alpha_0 = 30°$ (dia. 15 Å^{-1}). The dotted red lines mark the *k*-image planes. (d-f) Analogous simulations for $E_0 = 6$ keV (α_0 = 0 -14°; dia. 19 Å^{-1}). (d) Extractor mode [U_{Ex} = +20 kV; *F* = 2.5 kV/mm; dia. 12 Å^{-1}]. (e,f) Gaplens mode [U_{Ex} = +17 kV; U_R = -5 kV; *F* = 440 V/mm; dia. 19 Å^{-1}].

eV (Fig. 2), 900 eV and 6 keV (Fig. 3). 100 eV is achieved by synchrotron beamlines as well as HHG-based laboratory sources, while the latter two are typical soft and hard X-ray energies, respectively.

The trajectory simulations for $\boldsymbol{E_0} = \mathbf{100\ eV}$, Fig. 2, were performed for a range of take-off angles from $\alpha_0 = 0°$ to 70°. The *k*-field radius is given by $k_\parallel = 0.512 \sin\alpha \sqrt{E_0}$; 70° corresponds to a *k*-field diameter of 9.6 Å^{-1}. The simulation for the *extractor mode* is shown in Fig. 2(a). 20 kV at the extractor and ring electrode results in a homogeneous electric field of 3.3 kV/mm in a 6 mm gap. Fig. 2(b) shows the corresponding trajectories for the *gaplens mode*. By setting the ring electrode to U_R = -2 kV and reducing U_{Ex} to 15 kV, the homogeneous field is replaced by an accelerating lens in the gap between the sample and the extractor. The field strength at the sample is reduced to 1.2 kV/mm. It increases to 3.6 kV/mm at the center of the gaplens.

Spherical aberration causes the rays in a *k*-image to become increasingly over-focused as $k_\parallel$ increases, resulting in field curvature. On a planar detector, this field curvature causes image blur that increases with distance from the center. For most *k*-imaging experiments, the quantity of interest is not only the ultimate resolution Δk, but - equally important - the size of the *k*-field, which in many cases should contain more than a full Brillouin zone. Large *k*-fields are the main advantage of momentum microscopes, e.g. in comparison with hemispherical analyzers. Here we quantify the spherical aberration by a practical criterion: For a resolution value Δk we determine the maximum radius $k_\parallel^{max}$ up to which this resolution is achieved. For a given *k*-field, Δk is ultimately limited by the pixel resolution of the detector. Delay-line detectors with a 3D imaging scheme have effective pixel sizes of 80 µm. For an 80 mm detector this nominally corresponds to 1000 points along the image diameter (experiments typically yield half of this value). In the examples of Fig. 2, the photoemission horizon (defined by the full 2π solid angle) is about 10 Å^{-1}. Then 1000 resolved pixels correspond to a resolution of $\Delta k = 10^{-2}$ Å^{-1}, which we use as a quantitative criterion for the simulation. Note that this value is about a factor of 2 worse than the best *k*-resolution reported by Tusche et al. [14].

Ray tracing allows this criterion to be translated into a usable *k*-field diameter. Due to the *k*-image curvature the point (along the optical axis), at which two closely spaced ray bundles are just completely separated depends on the radius $k_\parallel$. The insets in Figs. 2(a) and (b) show black and blue ray bundles separated by 10^{-2} Å^{-1}. In the experiment, the focus is adjusted so that the image plane (dashed red line) intersects the point, where this condition is satisfied for the central (paraxial) and off-axis ray bundles (lower and upper insets). At these positions the rays are just separated at $\alpha_0 = 35°$ in (a) and 70° in (b), as shown in the upper insets, defining $k_\parallel^{max}$. $\alpha_0 = 70°$ (9.6 Å^{-1} diameter) in gaplens mode and $\alpha_0 = 35°$ (5.9 Å^{-1}) in extractor mode correspond to 94 % and 33 % of the full 2π solid angle, respectively. For $E_0 = 100$ eV the smaller field curvature in the gaplens mode gains about a factor of 3 in the accepted solid angle interval and 2.6 in the corresponding *k*-space area.

The divergence of the ray bundles is defined by the source diameter, defined by the photon footprint on the sample or the size of the field aperture. Here we assumed a spot of 30 µm diameter, which is a typical value for state-of-the-art HHG setups [27] and synchrotron beamlines [16,17]. $k_\parallel^{max}$ increases with decreasing source diameter. However, the field curvature does not depend on the source size, so the relative behavior remains the same. For extractor voltages < 20 kV, the curvature in (a) is even more pronounced, further reducing the usable angular range. The striking difference between Figs. 2(a,b) is also reflected in the spherical aberration coefficient C^k_3 of the reciprocal image. In the gaplens mode with field strengths of 1200 and 880 V/mm, this coefficient is about a factor of 3 smaller than in the extractor mode; see Table 1, values in blue and red boxes.

Two different effects are observed as a characteristic of ***chromatic aberration***. *Transverse chromatic aberration* (also called *chromatic aberration of magnification*) results in a variation of the image magnification as E_{kin} varies. This effect can be easily corrected numerically [23]. *Longitudinal chromatic aberration* results in a shift of the image plane because the refractive power of a lens varies with $1/\sqrt{E_{kin}}$. With increasing deviation from the chosen center energy this leads to image blur that cannot be corrected. These effects are present in real-space and *k*-images. They are negligible in experiments with HSA-based MMs or when studying core levels, due to the small transmitted energy band or the small linewidth. These effects become significant when imaging valence band patterns of several eV width with a ToF-MM. Especially in pump-probe experiments the ultrafast dynamics of both hot electrons (a few eV above E_F) as well as the corresponding holes (a few eV below E_F) must be simultaneously captured.

For the quantification of the chromatic aberration in gaplens mode we chose an interval of 100 ± 3 eV. Rays for different energies are shown in the insets of Fig. 2(c) in both the 1st *k*-image (left inset) and the 1st Gaussian image (right inset). The shift of the image plane (longitudinal effect) is negligible and not visible in the insets of Fig. 2(c). The *transverse* effect is quantified for $\alpha_0 = 30°$ in the left inset. Blue, black and red beams correspond to E_0 = 103, 100 and 97 eV, respectively. ΔE_{kin} = 3 eV results in a shift corresponding to 0.039 Å^{-1}, which can be

Table 1
Aberration coefficients for the lens geometry shown in Figs. 1(f,g) for an initial energy of $E_0 = 100$ eV. The electric field at the sample surface (Field) was varied in a wide range by adjusting the voltages of extractor (Ex) and ring electrode (R). M is the resulting image magnification. C_3 and C_C are the spherical and chromatic aberration coefficients and D_3 is the distortion coefficient of the Gaussian image. C^k_3 and C^k_C are the spherical and chromatic aberration coefficients of the reciprocal image. For the definition of the coefficients and details of their calculation see supplementary material.

	Field	Ex	R	M	C_3	C_C	D_3	C^k_3	C^k_C
MODE:	**V/mm**	**kV**	**kV**		**mm**	**mm**	**mm^{-2}**	**mm^{-2}**	
1. Extractor	3240	20	20	9.8	0.11	-0.19	0.039	0.24	0.20
2. Extractor	2400	15	15	10.1	0.20	-0.22	0.048	0.27	0.21
3. Extractor	1200	7.5	7.5	9.1	0.88	-0.44	0.086	0.27	0.28
4. Gaplens	1200	15	-2	11.3	0.17	-0.21	-0.045	0.10	0.075
5. Extractor	880	5.55	5.55	8.5	1.58	-0.62	0.107	0.27	0.33
6. Gaplens	880	10	0	10.3	0.36	-0.33	-0.033	0.09	0.092
7. Repeller	-14	9.3	-11.3	11.6	1.49	-1.14	-0.132	2.5	3.13

corrected by data processing [23]. This result is further quantified by the chromatic aberration coefficient C^k_C, which is a factor of 3.6 smaller in the gaplens mode than in the extractor mode (Tab. 1, last column).

In the *Gaussian image* the longitudinal effect is larger as shown in the right inset of Fig. 2(c). To avoid overlapping, the ray bundles (100 ± 3 eV in steps of 1 eV) were shifted laterally on the sample in steps of 200 nm. For $\Delta E_{kin} = 3$ eV the longitudinal effect results in a blur of 56 nm, which is in the range of the XPEEM resolution. However, XPEEM is typically performed at core levels with energy widths of < 1 eV, so the additional blur is < 10 nm and thus negligible. As with the *k*-image, the transverse effect can be corrected numerically [23]. We will return to the XPEEM mode in Sec. 3.

Simulations for the complete ToF-MM showed that these values for the spherical and chromatic aberration effects are transferred to the final *k*-image, see Fig. 2(d). The details of blue and black beams at the central (lower inset) and outer beam bundle (upper inset) in the final *k*-image in Fig. 2(d) show the same *k*-resolution as found for the 1st *k*-image in Fig. 2 (b). These results for $E_0 = 100$ eV have shown that the gaplens mode provides access to the full 2π solid angle interval, which typically includes many Brillouin zones. A wide range of applications is expected.

The results for $\boldsymbol{E_0 = 900}$ **eV** ($\alpha_0 = 0$-30°) **and 6 keV** ($\alpha_0 = 0$-14°) are shown in Fig. 3. As a consequence of the larger *k*-field diameters of 15 and 19 Å^{-1}, the field curvatures in the *extractor mode* (denoted by the dashed red curves in Figs. 3(a) and (d)) are even larger and lead to blurring of the outer parts of the images. The usable angular range defined by 1000 resolved image points is reduced to 20° (*k*-field diameter of ~10 Å^{-1}) for 900 eV and 9° (diameter ~12 Å^{-1}) for 6 keV. The trajectories for the *gaplens mode* at 900 eV are shown in Figs. 3(b,c). In this case, the total *k*-field of 15 Å^{-1} satisfies the condition $\Delta k = 0.015$ Å^{-1}. Here, the field strength is 1.3 kV/mm at the sample and increases to 3.8 kV/mm at the center of the gaplens.

For $E_0 = 6$ keV the gap size was increased to 8 mm, which proved to be advantageous for experiments at such high energies. Due to the larger *k*-field the usable angular range is defined by the criterion $\Delta k = 0.02$ Å^{-1}. For the *gaplens mode* with $U_{Ex} = 17$ kV and $U_R = -5$ kV the entire *k*-field of 19 Å^{-1} satisfies this condition (Fig. 3(e)). The *k*-field curvature is very small and the field strength at the sample is as low as 440 V/mm, see Fig. 3(f). It can be reduced to zero for a larger negative potential at R, as will be discussed in the following section. Such settings are optimal for operando samples with contacts or actuators on the surface. By providing access to *k*-fields of up to 20 Å^{-1} in diameter, the gaplens mode is advantageous for hard X-ray XPD studies. Such large $k_{\|}$-values require the incorporation of subsequent electron lenses with larger diameters while maintaining reasonable fill factors.

It can be concluded that the additional lens positioned between the extractor and the sample has the effect of reducing the field strength at the sample surface compared to the extractor mode. In addition, the *k*-field diameter is increased and the *k*-resolution is improved over the entire energy range from the XUV to hard X-rays. We have introduced the practical criterion that the *k*-resolution should be limited by the detector resolution and not by the electron optics. The combination of a reduced field at the sample and improved image quality makes the gaplens mode a promising option for many applications. It is the standard mode at the HHG-based fs XUV source at CELIA, Bordeaux [27–29]. It has also been used in soft X-ray experiments at beamline P04 at PETRA III (DESY, Hamburg, Germany) [30,31].

2.3. Repeller and zero-field mode

By setting the ring electrode R to a larger negative voltage and reducing U_{Ex} the field at the sample surface can be tuned to zero or even negative values. Such modes are called *zero-field* and *repeller modes*. The gaplens mode (see Section 2.2) is a flexible alternative to the conventional extractor mode. In contrast, the *repeller mode* is primarily designed for a specific application, namely the reduction of space charge interaction. Consequently, this mode is particularly attractive for time-resolved photoelectron momentum microscopy using pump-probe techniques. In these experiments, a significant number of slow electrons can be emitted by the pump pulse through nPPE processes or plasmonic emission. Time-resolved ToF-MM at FELs and HHG-based laboratory sources is an emerging technique that is on the rise. References [28,29,32–38] provide insight into various aspects of this technique.

Fig. 4 shows the *repeller mode* for four initial energies between $E_0 =$ 36 eV and 3.6 keV. In this range, the extractor potential is reduced from $U_{Ex} = +9.5$ kV to +3.3 kV, and $U_R = -12$ kV for the first three cases and -15 kV for 3.6 keV, resulting in repeller fields at the sample surface between $F = -11$ V/mm and -1.3 kV/mm, respectively. The retarding field determines the distance at which electrons of a given energy are repelled toward the sample surface. The saddle point acts as a high-pass filter, with U_S defining the cutoff energy for the electrons escaping from the sample. In the sequence from $E_0 = 36$ eV to 3.6 keV, the cutoff energy increases from 3 eV to 3.15 keV; see values in the panels of Fig. 4. The refractive power of the saddle point potential is very high, so the first *k*-image is located in the gap region and the first Gaussian image appears close to the extractor bore. The real-space imaging properties of this unusual type of lens will be discussed in Sec. 3.

Fig. 4(a) shows the front lens region up to the 2nd *k*-image, while (b)

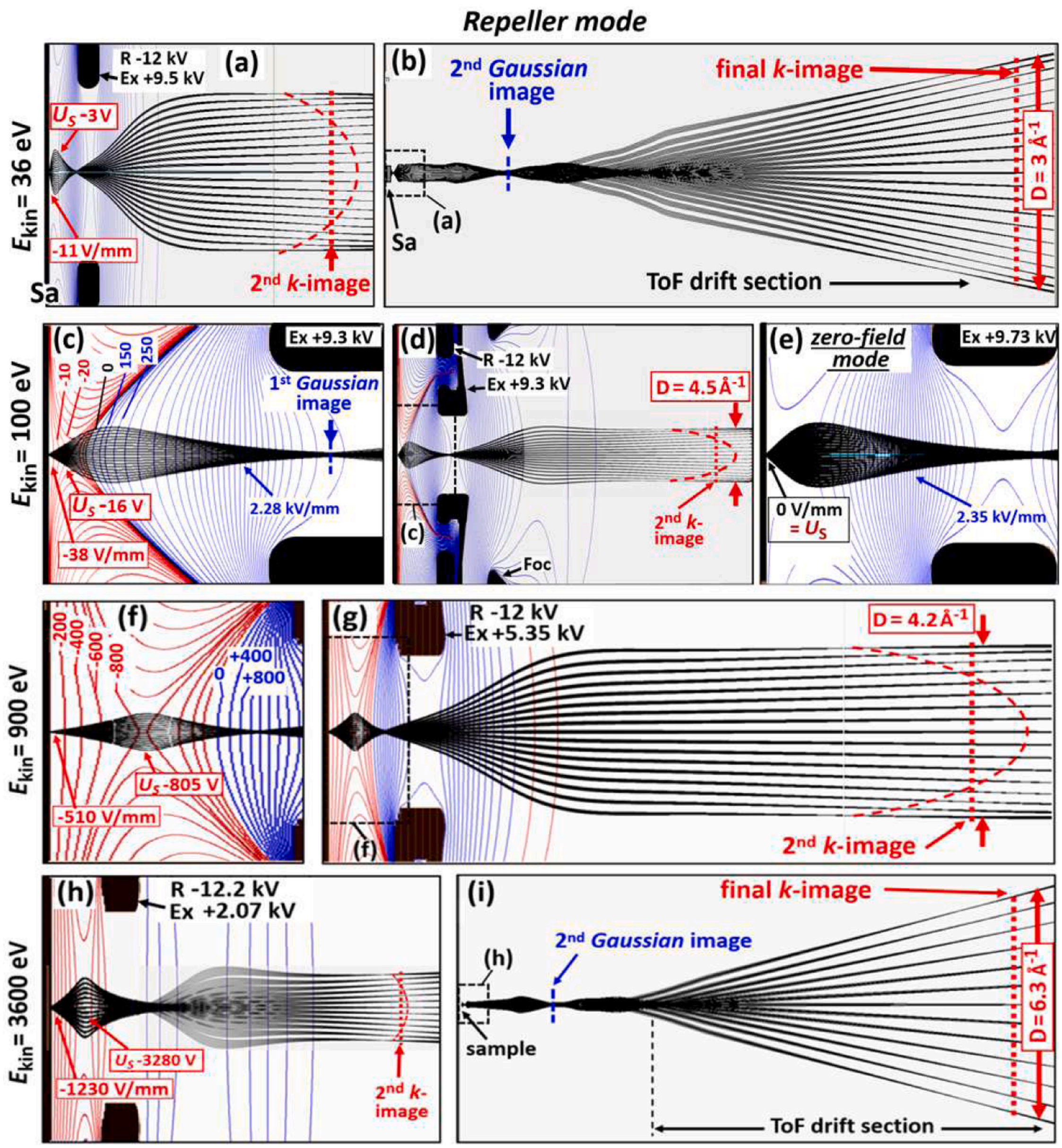

Fig. 4. Ray tracing for the *repeller mode* and the *zero-field mode* (only (e)). The retarding field F at the sample surface and the potential of the saddle point U_S are given in the panels. (a,b) *Repeller mode* for $E_0 = 36$ eV and $\alpha_0 = 0$-30°, corresponding to a k-field of 3 Å^{-1} diameter. (a) Detail from sample (Sa) to the 2nd k-image; (b) simulation for full ToF MM optics. (c,d) The same for $E_0 = 100$ eV for $\alpha_0 = 0$ -27° (k-field 4.5 Å^{-1}). The retarding and accelerating field regions are marked by red and blue equipotential contours, respectively; the numbers represent the potential in volts. (e) *Zero-field mode* obtained from (d) by increasing U_{Ex} by 430 V. (f,g) *Repeller mode* for $E_0 = 900$ eV and $\alpha_0 = 0$ - 8° (k-field 4.2 Å^{-1}). (h,i) Simulation for $E_0 = 3.6$ keV and $\alpha_0 = 0$ - 6° (diameter 6.3 Å^{-1}).

shows the complete lens optics of a ToF-MM for $E_0 = 36$ eV and $\alpha_0 = 0$ - 30° (k-field diameter 3 Å^{-1}). The simulation for the complete ToF MM optics shows that the k-field visible in (a) is transferred to the final k-image on the detector, i.e., the aberrations of the following lenses are not significant. This configuration with U_S = -3 V effectively removes all slow electrons with kinetic energies up to 3 eV from the beam. Fig. 4(c) shows the equipotential contours of the front lens for $E_0 = 100$ eV and $\alpha_0 = 0$ - 27° (diameter 4.5 Å^{-1}). The contours of the retarding region are shown in red. The retarding field of F = -38 V/mm causes slow electrons with energies up to 3.8 eV to turn back within the first 100 μm from the surface. Up to the saddle point at U_S = -16 V all electrons up to $E_0 = 16$ eV are repelled.

Increasing U_{Ex} to +9.73 kV causes the saddle point to shift toward the sample surface, establishing the *zero-field mode,* see Fig. 4(e). Under these conditions, the field increases gradually and remains relatively low for the first half mm. This is advantageous for samples with 3-dimensional structures, such as operando devices with electrodes on the top surface. For clarity, the voltages on the potential contours in Fig. 4 and on the lens elements in all Fig.s are referenced to the sample (i.e. $U_{Sa} = 0$). In experiments U_{Sa} is often set to E_0/e. The shapes of potential contours and trajectories do not depend on the choice of reference point.

With increasing kinetic energy, the basic behavior remains the same, as can be seen in the results for 900 eV and 3600 eV shown in Figs. 4(f,g) and (h,i), respectively. To maintain the high refractive power at higher kinetic energies, U_{Ex} is reduced and U_R is increased (for $E_0 = 3.6$ keV, U_R = -15 kV and U_{Ex} = +3.3 kV). We observe a trend that the saddle point and the first k-image move closer to the extractor hole and the usable k-field diameter increases. The strong deceleration and the curvature of the equipotential contours act as a strong lens. In Fig. 4(h) E_{kin} drops from 3.6 keV at the sample to 320 eV at the saddle point. The distance between the object (sample) and the first Gaussian image is between 5 and 10 mm.

The lens geometry is designed so that the position of the second k-image in the repeller mode coincides with the position of the first k-image in gaplens and extractor modes. In the microscope, this plane contains the array of contrast apertures. The usable k-field diameter is reduced compared to the other modes. However, it increases with increasing kinetic energy, from 3 to 6.3 Å^{-1} in the sequence in Figs. 4(b, d,g,i). This reduction in the k-field size is also reflected in an order of magnitude larger spherical aberration coefficient C^k_3 of the reciprocal image (Tab. 1, last row).

2.4. Basics of the repeller mode

The crucial effect of the *repeller mode* is the fast separation of the slow background electrons from the photoelectrons. Here we briefly recall the essentials from Fig. 2 of Ref. [39]. Early time-resolved ARPES experiments at FELs [40,41] have shown that both the pump and the probe pulses contribute to the space charge effects. Simulations and synchrotron experiments [10] as well as FEL experiments [11,39] have shown that the situation is particularly critical in the *extractor mode,* because the field accelerates the slow electrons into the lens column, where they travel as a charge cloud along the optical axis at a short distance from the photoelectrons. The integral Coulomb interaction along the optical path causes artifacts in time-resolved measurements, masking the true dynamic effects.

Zhou et al. [42] were the first to analyze the combined effect of space charge and image charge for excitation with 60 ps synchrotron pulses. For such long pulses the electron cloud is propagated along the optical axis. Nevertheless, the study showed that the effect of the space charge and its positive image charge (also called mirror charge) induced in the conducting surface partially compensate each other. Femtosecond pump pulses release slow electrons that form a flat 'charge carpet' in front of the surface (Fig. 2(a) of [39]). In *repeller mode*, this charge carpet remains close to the surface for hundreds of ps (Fig. 4 of [39]). However, the positive image charge effectively shields the Coulomb forces. For the flat charge carpet, the configuration resembles the field of a capacitor. The photoelectrons emitted at a later time by the probe pulse pass through this carpet of slow electrons within a short time (a few to a few tens of ps), depending on their energy. After passing through the carpet, the escaping photoelectrons 'see' only the far-field distribution of this capacitor. What remains is the stochastic e-e scattering as the photoelectrons (typically very few per photon pulse) cross the high-density charge carpet. These stochastic events kick the electron out of the observed phase space volume [43] and only contribute to a diffuse background at lower energies.

Prior to the development of the multimode lens, we gained initial experience with the so-called *long-range modes* that are possible in any MM or PEEM with an electrostatic cathode lens. When the extractor is at the same potential as the sample, the *long range zero field mode* is formed. This mode has been exploited when tilting the sample in order to record patterns at large off-normal angles (see Fig. 2(c) in [17] and Figs. 5(j-p) in [19] for details). When the extractor is set at a negative potential with respect to the sample, the *long-range repeller mode* is obtained. The operation of this mode was previously confirmed in an experiment at the FEL FLASH at DESY [39], and it has been successfully used to probe sub-picosecond magnetization dynamics [32].

In summary, the *repeller mode* is mainly useful in cases where space charge effects are a significant obstacle. In pump-probe experiments it provides access to a regime of pump fluences that is prohibitive for both, MMs in extractor mode [39] and conventional hemisphere-based ARPES experiments [40,41]. The strength of the space charge effects depends on many factors, the discussion of which is beyond the scope of this article. In general, it is less severe for sources with high pulse rates, such as the cavity-enhanced HHG sources [44].

3. Real space imaging

3.1. ToF XPEEM mode

The ability to obtain high quality PEEM images with momentum microscopes is important for a number of applications. Obviously, PEEM is an effective way to optimize the photon footprint on the sample and the spatial overlap of the pump and probe beams; an example is shown in Ref. [11]. Second, the identification of homogeneous regions for k-imaging is particularly important in the context of cleaved samples. Third, the detection and subsequent elimination of emission hot spots from the region of interest (ROI) by lateral displacement is of paramount importance in pump-probe experiments. The intense electron emission from hot spots is a major source of space charge effects. Fourth, PEEM imaging is critical for the *small-ROI mode* of momentum microscopy, analogous to *sub-micron ARPES*. The ROI can be limited by a small field aperture in the intermediate Gaussian image. The effective emission

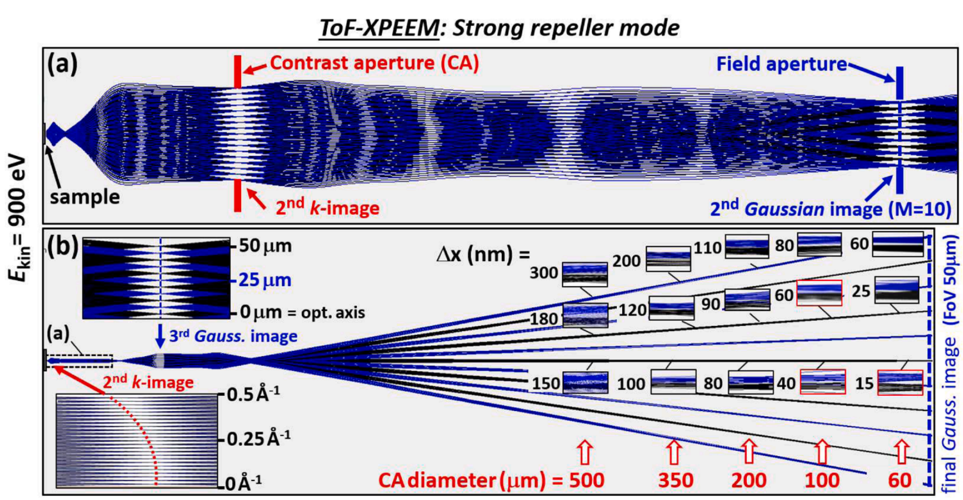

Fig. 5. Time-of-flight XPEEM simulations for $E_0 = 900$ eV using the *repeller mode* [$U_{Ex} = 5.35$ kV, $U_R = -12$ kV, $F = -510$ V/mm]. (a) Front section showing the 2nd momentum and 2nd Gaussian images aligned to the planes containing the contrast and field aperture arrays. These planes host the 1st k-space and Gaussian images in extractor and gaplens modes. (b) Rays for the complete microscope optics at high magnification ($M_{tot} = 1600$). The upper and lower insets on the left show the details of the 3rd Gaussian and 2nd k-image, respectively. The small insets on the right show ray groups starting from the sample at distances Δx between 300 and 15 nm; the corresponding CA diameters are given at the bottom. High resolutions of 50 nm or better are achieved only for reduced FoV of 20 µm diameter, see second row of insets.

area for k-image acquisition is defined by this aperture, independent of the photon footprint. ROIs of 700 nm in diameter have been selected for k-imaging using UV laser excitation, with a photon footprint of approximately 20 μm [45]. Even smaller ROIs appear to be feasible, provided that the photon flux in the ROI is sufficiently high.

The four applications mentioned above support measurements of k-distributions. In addition, high-quality real-space imaging facilitates efficient analysis of the surface chemical structure. In a seminal paper, Tonner [46] proposed a HSA-based energy-filtered PEEM for the X-ray region (XPEEM). This concept was subsequently demonstrated experimentally using synchrotron radiation by Bauer and coworkers [47]. Later, the method was extended to higher energies using double-hemisphere setups [48,49,9]. These approaches are 2-D recording methods. A ToF-MM can record 3-D data arrays (x,y,E_{kin}), allowing rapid mapping of the chemical structure of a sample. The high chemical sensitivity of ToF-XPEEM allows the determination of the atomic species and their chemical states via core-level shifts.

Locatelli et al. [7] were the first to observe that the spatial resolution of XPEEM at synchrotron sources is ultimately limited by space charge effects. Later it was shown that this is also the case for aberration-corrected instruments [8]. For metallic samples, the secondary electron spectrum resulting from the keV primary electrons exhibits a peak at about E_{kin}= 2 eV and a width of several eV, which depends on the work function (for details, see Ref. [50]). The secondary electron background due to cascade scattering effects increases strongly with increasing E_0. A ToF-MM experiment at E_0 = 1 keV using synchrotron radiation from a soft X-ray beamline provided a quantitative assessment of this phenomenon [10]. Space charge shifts > 10 eV indicate the presence of a macrocharge of 10^5-10^6 slow electrons trailing each photoelectron. The Coulomb repulsion is sustained over long periods of time and acts over macroscopic distances of tens of mm. By removing all slow electrons from the beam very close to the sample surface, the *repeller mode* is expected to dramatically improve XPEEM performance in the soft and even more so in the hard X-ray region.

We have performed XPEEM simulations in repeller mode at various energies from EUV to hard X-rays. As an example, Fig. 5 shows results for E_0 = 900 eV. Voltages U_R and U_{Ex} were identical to Fig. 4(f), which shows trajectories and equipotential lines of the special field distribution near the sample. The strong retarding field of F = -510 V/mm removes all electrons with $E_0 \leq 5$ eV from the beam within the first 10 μm above the sample. Following the results of Refs. [10,39] this should have the effect of 'turning off' the Coulomb forces exerted by the slow electron macrocharge. The trajectories up to the 2nd Gaussian image are shown in Fig. 5(a). The positions of the contrast aperture and the field aperture, which are used to limit the k-range and the real-space range, respectively, are indicated. The lenses are adjusted so that these positions coincide with those of the 1st momentum and Gaussian images in extractor and gaplens modes. This coincidence allows switching between the modes simply by varying the lens excitations.

Fig. 5(b) shows a simulation for the entire column with the lenses set to a high magnification (M_{tot} = 1600). Systematic simulations revealed that such strong retarding field settings are characterized by a negligible curvature of the Gaussian image. An example for a FoV of 100 μm is shown in the upper left inset of Fig. 5(b). We can speculate that this is a property of the saddle-point field distribution, examples see Figs. 4(c,f, h), which is atypical for converging lenses. However, this planar Gaussian image comes at the cost of an increase of the k-field curvature, as shown in the lower left inset of Fig. 5(b). This strong k-field curvature is the reason for a significant reduction of the observable k-field diameter in repeller mode.

We investigated the theoretical XPEEM resolution of the repeller mode using the same approach as for k-imaging (see Fig. 2). The black and blue groups of rays in the insets to the right of Fig. 5(b) are separated on the sample by the distance Δx as indicated. The five columns correspond to different sizes of the contrast aperture CA between 500 and 60 μm as indicated at the bottom. Due to the small field curvature, all insets in Fig. 5(b) are at or near the detector plane, dashed blue line on the right. For each CA size, the spatial resolution is determined as the value of Δx, where the ray bundles are just resolved. Due to the spherical aberration, Δx increases with increasing distance from the optical axis. Here we show Δx values for the paraxial rays (bottom row of insets), for the edge of a 20 μm FoV (middle row) and for the edge of a 50 μm FoV (top row). As CA is reduced, Δx varies from 150 to 15 nm on the optical axis, from 180 to 25 nm at the edge of the 20 μm FoV and from 300 to 60 nm at the edge of the 50 μm FoV. The 1000-pixel criterion gives 20 nm for 20 μm FoV and 50 nm for 50 μm FoV. This means that the CA 60 μm achieves pixel resolution for these fields of view.

In summary, these simulations indicate that an XPEEM resolution of < 20 nm can be achieved in *repeller mode*, where the space charge effects are expected to be negligible. As the diameter of the contrast aperture is reduced from 500 to 60 μm, the cross-section of the central ray bundle shrinks from Δx = 150 nm to 15 nm. The spherical aberration coefficient C_3 of the repeller mode is almost identical to that of the extractor mode at 880 V/mm; compare rows 5 and 7 of Tab. 1. In contrast, the coefficients of the k-image C^k_3 and C^k_C are an order of magnitude larger for the repeller mode.

Experimentally, a prototype ToF-MM with multimode front lens achieved a resolution of 90 nm by imaging triangular flakes of V-doped WS_2 at the W 4*f* core level with soft X-rays at beamline P04 (PETRA III, DESY, Hamburg) [51]. The optics were operated in gaplens mode and the transverse chromatic aberration was numerically corrected. This value is comparable to nano-ARPES experiments with hemispherical analyzers and small-spot photon beams using Kirkpatrick-Baez optics and/or zone plates, e.g. at the 'MAESTRO beamline' [52] (at the ALS, Berkeley) or the 'ANTARES beamline' [53] (at Soleil, Saint-Aubin). A spectroscopic XPEEM without aberration correction ('SPELEEM' at ELETTRA, Trieste) achieved a resolution of 30 to 40 nm [7]. An aberration-corrected instrument ('SMART' at BESSY, Berlin) reached a resolution of 18 nm [8]. In the LEEM mode with continuous beam, the same instrument reached 2.6 nm, indicating that 18 nm is still limited by space charge interactions in front of the small contrast aperture.

Such experiments require a large lateral magnification and a sufficiently high flux density in the photon footprint. At the hard X-ray beamline P22 of PETRA III, photon spot sizes < 10 μm have been achieved by using a focusing X-ray capillary [54]. This flux density will allow to elucidate the practical limit of ToF-XPEEM resolution. The hard X-ray region is highly attractive due to the large mean free path of the photoelectrons, which allows the study of buried structures and thin film devices [55,56] even in operando.

3.2. ToF-PAXRIXS mode

Finally, we introduce an upcoming application of the multimode front lens that will offer a new approach to Resonant Inelastic X-ray Scattering (RIXS). Fig. 6 shows the results of an XPEEM simulation in *gaplens mode* to elucidate the maximum possible field of view. We found diameters exceeding 4 mm, which is five times larger than the FoVs achievable with standard low-energy PEEMs and MMs. These large fields are paramount for a forthcoming methodology in which the inelastically scattered X-ray photons impinge on a thin converter foil, releasing photoelectrons. The photoelectron spectrum reflects the X-ray spectrum, hence the name *Photoelectron spectrometry for Analysis of X-rays* (PAX). Until now, PAXRIXS has been measured using classical hemispherical spectrometers [12,57]. In the new ToF-PAXRIXS approach, the microscope will capture 3D photoelectron arrays I(E_{kin}, *x,y*) from the converter foil with highest efficiency. The E_{kin} distribution reflects the energy loss spectrum of the X-rays and the lateral coordinates (*x,y*) are a measure for the momentum transfer. Since typical RIXS energies are in the soft X-ray range, we ran the simulation for E_0 = 900 eV.

Fig. 6(a) shows the region near the sample. The gap lens field contracts the ray bundles and pulls the outer bundles closer to the optical

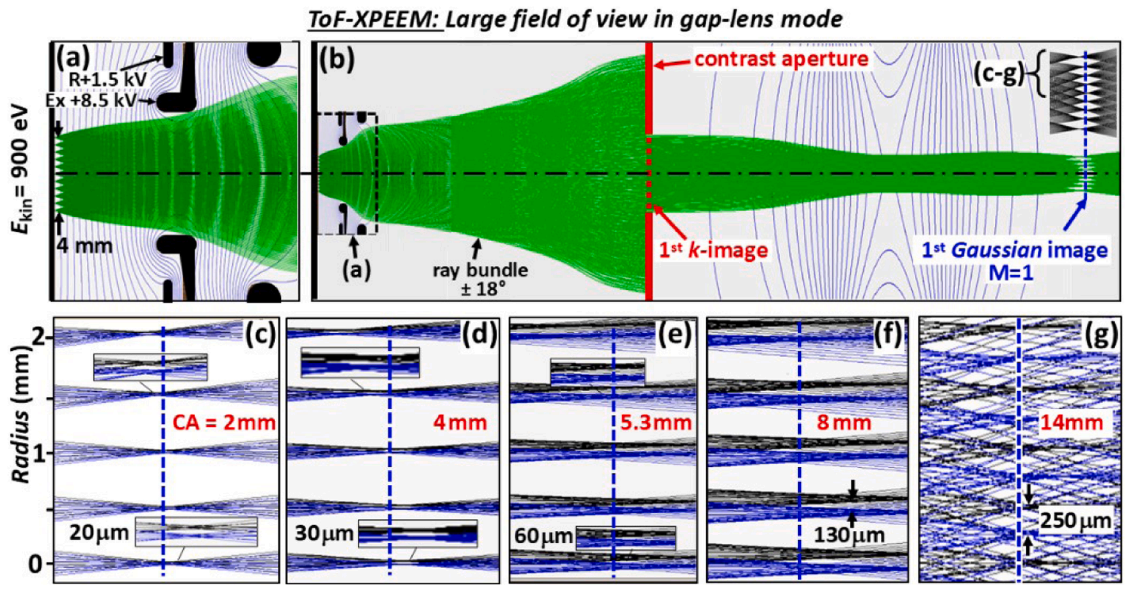

Fig. 6. Time-of-flight XPEEM simulations for $E_0 = 900$ eV and a field of view of 4 mm using the *gaplens mode* [$U_{Ex} = 8.5$ kV, $U_R = +1.5$ kV, $F = 630$ V/mm]. (a) Front part showing how the ray bundles in the interval $\alpha_0 = 0$ - 18° (*k*-field 9.3 Å^{-1}) are contracted by the gaplens field. (b) Rays up to the 1st Gaussian image at a magnification of M = 1, which requires a different position and a large size of the contrast apertures. The curved stripes in (a) are moiré artifacts. (c-g) Details of the Gaussian images simulated for contrast aperture diameters between 2 and 14 mm as indicated. The panels show black and blue ray groups starting from the sample at distances Δx between 20 μm (c) and 250 μm (g).

axis. For this simulation, the extractor hole diameter was increased to 5 mm so that all rays originating from the 4 mm FoV with $\alpha_0 = 0$ - 18° would pass through the hole. Fig. 6(b) shows the rays up to the first Gaussian image. The small magnification (here M=1) requires a large diameter for the first *k*-image. Thus, this instrument has a contrast aperture array in a different position and larger apertures up to 14 mm. The final magnification at the detector is $M_{tot} = 17$, allowing observation of a 4.7 mm FoV on an 80-mm-diameter detector. Performance criteria for this application include a large FoV diameter to capture a broad range of momentum transfer and acceptance of a large solid angle defined by the contrast aperture. To observe the *k*-dispersion in RIXS, 20 to 40 resolved points along the image diameter are sufficient.

Fig. 6(c-g) show an enlarged section of the Gaussian image shown in the small inset on the top right side of (b). This region extends from radius 0 to 2 mm of the FoV, see the ordinate scale in (c). Patterns (c,d,e, f,g) were determined using contrast apertures of 2, 4, 5.3, 8 and 14 mm, respectively. The sizes of the CAs and the distances of the blue and black ray bundles are given in the panels. The results for small CAs were used to check the resolution limit. 20 μm, as found for CA 2 mm (c), corresponds to 200 resolved points along the diameter of the FoV. For PAX-RIXS high intensity is mandatory; therefore the optimal operating point will be at large CA diameters that are just sufficient for the required lateral resolution. Figs. 6(f) and (g) show simulations with CAs of 8 and 14 mm, yielding 130 μm and 200 μm, respectively. These correspond to 30 and 20 resolved points along the FoV diameter. For the 14 mm case (g), the diffuse background increases significantly; thus, this appears to be the practical limit. This value corresponds to $\alpha_0 = 0$ - 8°, which is a typical acceptance range of hemispherical analyzers. Such analyzers record the distribution along a line. In contrast, the ToF-PAXRIXS approach simultaneously captures the full 2D ROI with a radius of 2 mm. We have not yet determined the aberration coefficients for $E_0 =$ 900 eV, but we expect them to follow the same trend as those for 100 eV. In gaplens mode, C_3 is a factor of 4 - 5 smaller than in extractor mode (Tab. 1, rows 3-6).

4. Summary and conclusions

A novel front lens has been developed for photoelectron momentum microscopes and PEEMs. The primary goal was to reduce the electric field strength at the sample surface thereby lowering the risk of field emission or flashovers. These occurrences can be caused by local field enhancement at sharp corners or protrusions of cleaved samples. A second goal was to create a retarding field at the surface. In soft and hard X-ray excitation and pump-probe experiments, the charge cloud of slow background electrons is the main source of space charge effects. Redirecting all slow electrons back to the surface largely eliminates these effects.

Systematic ray tracing calculations were performed for different geometries. One or two annular electrodes that are concentric to the extractor provide the degree of freedom to shape the electric field. The result is a lens design that allows for four modes of operation: *Extractor mode,* which operates with a high accelerating field; *gaplens mode*, which operates with a significantly reduced field strength, *zero-field mode,* in which the field at the sample is tuned to zero; and *repeller mode*, which operates with a retarding field at the surface. The key design criterion was that all four modes could be selected by simply applying different potentials to the lens elements while keeping their geometry and the position of the contrast aperture mechanism fixed. Since the retarding field has a strong refractive power, this criterion could only be met by adjusting the second *k*-image of the repeller mode to the position of the first *k*-image of the other modes. In addition to ray tracing, we determined the aberration coefficients of the real-space and *k*-space images.

Adjusting the ring electrodes to a lower potential reduces the electric field *F* at the sample from the typical range of 3 - 10 kV/mm in extractor mode to 0.4 - 1.5 kV/mm. This greatly reduces the likelihood of field emission or flashovers because these phenomena often exhibit threshold behavior as a function of *F*. The extractor electrode, which is at a high positive voltage and is surrounded by annular electrodes at lower voltages, forms a gap lens between the sample and the electrodes. In *gaplens mode* the field curvature of the *k*-image in the back focal plane is significantly reduced, and the depth of focus increases. Each resolution value, Δ*k,* defines a maximum radius, $k_{\parallel}^{max}$, up to which this resolution is achieved. For our comparative study, we chose $E_0 = 100$ eV, an energy available at synchrotrons and HHG-based laboratory sources. A resolution of $\Delta k = 10^{-2}$ Å^{-1} is obtained for 94 % of the full 2π solid angle (diameter 9.6 Å^{-1}) in gaplens mode and for only 33 % (diameter 5.9 Å^{-1})

in extractor mode (see Figs. 2a and 2b). Consistent with this result, the aberration coefficient C^k_3 of the *k*-image is approximately a factor of 3 smaller in gaplens mode than in extractor mode.

The advantages of the *gaplens mode* become even more significant at higher kinetic energies. Its low aberrations enable imaging of *k*-fields up to 20 $Å^{-1}$, which is crucial for XPD experiments [18,19]. Large areas are also accessible in XPEEM mode. For example, a 4 mm FoV was achieved at $E_0 = 900$ eV. This will be crucial for the upcoming ToF-PAXRIXS technique [12,57]. The *zero-field mode* provides access to large off-normal emission angles via sample tilt [17,19]. Due to the vanishing field strength at the sample surface, this mode is ideal for samples with surface roughness, corrugations, or 3D structure. Such topographic effects deform the electrostatic field and degrade resolution [58,59].

Current experiments using an HHG source with a low kinetic energy of 16 eV standardly use the gaplens mode [27–29]. It has also performed well with soft X-rays at the PETRA III synchrotron [30,31]. A key feature contributing to the high collection efficiency is the small distance between the gap lens and the sample. Its high refractive power and proximity to the object mimic the characteristics of an objective lens in an optical microscope. The gap lens is followed by an aperture lens (the extractor hole), which has negative aberration coefficients [60]. Unlike in optical microscopy, round lenses in particle optics cannot eliminate spherical aberration, as demonstrated by Scherzer and Rose [61,62].

Applying a negative potential to the ring electrode(s) creates a retarding field at the sample surface. Slow electrons up to a certain cutoff energy are deflected back to the surface, hence the name *repeller mode*. The number of slow secondary electrons can exceed the number of photoelectrons by several orders of magnitude, as quantified at 1 keV in Ref. [10]. In pump-probe experiments, the pump pulse can produce large numbers of slow electrons via nPPE processes. Present ray tracing calculations and aberration coefficients quantitatively support previous qualitative considerations regarding the reduction of space charge effects [10,26,39,43]. Eliminating the primary source of Coulomb forces enables pump fluences that were previously unattainable. It paves the way for a promising future of the *repeller mode* in time-resolved pump-probe experiments. This is particularly important for experiments at X-ray FELs, which involve both high photoelectron energies <u>and</u> slow electrons released by the pump pulse. The first iteration of the repeller mode, in which the extractor served as the repeller electrode, was investigated at the FEL FLASH at DESY [39] and was subsequently used in experiments [32,33]. Initial experiments with an HHG source revealed that the repeller mode remains effective at kinetic energies as low as 16 eV [13]. However, the recorded *k*-field diameter is smaller, and chromatic aberration is larger.

Previous synchrotron experiments [7–9] have shown that the resolution in XPEEM is limited by space charge effects. Therefore, eliminating the space charge effects in real-space imaging using the *repeller mode* should be advantageous. While transverse chromatic aberration (i.e. the variation of image magnification with energy) can be corrected numerically [23], longitudinal chromatic aberration (i.e., the shift of the focal plane) cannot. However, this is not a significant problem for XPD and XPEEM at core levels, since the width of the signals is typically less than 1 eV. For valence band mapping in ToF-MM the shift of the focal plane can pose an obstacle, requiring the acquisition of several smaller energy intervals with appropriate refocusing for each interval. Despite the repeller mode's large overall aberration coefficients, Fig. 5(b) predicts resolutions of 60 nm for a FoV of 50 μm and even 25 nm for a FoV of 20 μm. Using soft X-rays from PETRA III (DESY, Hamburg), WS_2 flakes have been imaged at the W 4*f* core level in *gaplens mode* with a resolution of 90 nm [51]. This value was limited by the pixel resolution of the detector.

The key messages of the aberration coefficients in Table 1 can be summarized as follows: For PEEM imaging, the classical extractor mode with strong electric field at the sample surface is superior (smallest C_3 and C_C) if field emission, flashovers, and space charge effects are not an issue. However, this is not the case for *k*-imaging, because even with extractor 20 kV (row 1) the C^k_3 and C^k_C coefficients are still significantly larger than those of the gaplens mode at much lower fields (rows 4 and 6). At reduced fields all aberration coefficients are smaller in the gaplens mode for both Gaussian <u>and</u> *k*-space imaging (see values for 1200 and 880 V/mm). Finally, the imaging performance of the repeller mode is moderate for Gaussian imaging and poor for *k*-imaging compared to all other modes. This is the price we pay for eliminating the effects of space charge. The usefulness of the repeller mode depends on the trade-off between space charge effects and loss of imaging performance.

In summary, the novel front lens configuration offers operating modes that are not possible with conventional cathode lenses. Two features in particular make this lens attractive. First, a significantly reduced electric field at the sample avoids field emission and flashovers, which are particularly severe for cleaved samples. Second, a retarding field can redirect slow electrons back to the surface, eliminating the main source of space charge effects that can degrade energy and *k*-resolution. An overview of initial experiments can be found in Refs. [13] and [27].

CRediT authorship contribution statement

Olena Tkach: Writing – original draft, Data curation. **Gerd Schönhense:** Writing – original draft, Data curation.

Declaration of competing interest

The authors declare the following financial interests/personal relationships which may be considered as potential competing interests:

Schoenhense Gerd, Schoenhense Benedikt Marian has patent ARRANGEMENT FOR THE REDUCTION OF THE SPACE CHARGE INTERACTION IN ELECTRON SPECTROSCOPIC DEVICES issued to DE 10 2017 126 882 B3 2019.01.10. If there are other authors, they declare that they have no known competing financial interests or personal relationships that could have appeared to influence the work reported in this paper.

Acknowledgements

We thank H.-J. Elmers, O. Fedchenko and Y. Lytvynenko (Mainz Univ.), S. Beaulieu, S. Fragkos and Y. Mairesse (CELIA, Bordeaux), T. Allison (Stony Brook Univ.), S. Chernov, C. Schlueter, M. Hoesch, D. Kutnyakhov, M. Scholz and K. Rossnagel (DESY, Hamburg), Q. Nguyen (SLAC, Stanford) and B. Schönhense (Springbok.ai) for fruitful discussions on various aspects of this article. Special thanks are due to Ruud Tromp (Leiden Univ.) for his advice on determining lens aberrations; to Roland Janzen (Janzen Consulting, www.dr-janzen.de) for incorporating the calculation of aberration coefficients into his program JSAAP; and to Alice Kunin (Princeton Univ.) for her careful review of the manuscript. This development was funded by the BMBF (projects 05K22UM1, 05K22UM2 and 05K22UM4) and the Deutsche Forschungsgemeinschaft DFG (German Research Foundation) through TRR 173-268565370 Spin+X (project A02) and project No. Scho341/16-1. We are sad to say goodbye to Takanori Koshikawa, who promoted our field of research far beyond Japan's borders for decades.

Supplementary materials

Supplementary material associated with this article can be found, in the online version, at doi:10.1016/j.ultramic.2025.114167.

Data availability

Data will be made available on request.

References

[1] E. Brüche, Die Auflösungsgrenze des Emissions-Elektronenmikroskops, Kolloid-Zeitschrift 100 (1942) 192–206, https://doi.org/10.1007/BF01519547.

[2] A. Recknagel, Das Auflösungsvermögen des Elektronenmikroskops für Selbststrahler, Z. Physik 120 (1943) 331–362, https://doi.org/10.1007/BF01325849.

[3] E. Bauer, The resolution of the low energy electron reflection microscope, Ultramicrosc. 17 (1985) 51, https://doi.org/10.1016/0304-3991(85)90176-7.

[4] G.F. Rempfer, O.H. Griffith, The resolution of photoelectron microscopes with UV, X-ray and synchrotron excitation sources, Ultramicrosc 27 (1989) 273–300, https://doi.org/10.1016/0304-3991(89)90019-3.

[5] R.M. Tromp, Measuring and correcting aberrations of a cathode objective lens, Ultramicrosc 111 (2011) 273, https://doi.org/10.1016/j.ultramic.2010.11.029.

[6] R.M. Tromp, W. Wan, S.M. Schramm, Aberrations of the cathode objective lens up to fifth order, Ultramicrosc. 119 (2012) 33, https://doi.org/10.1016/j.ultramic.2011.09.011.

[7] A. Locatelli, T.O. Mentes, M.Á. Niño, E. Bauer, Image blur and energy broadening effects in XPEEM, Ultramicrosc. 111 (2011) 1447, https://doi.org/10.1016/j.ultramic.2010.12.020, see also, https://www.elettra.eu/it/lightsources/elettra/elettra-beamlines/nanospectroscopy/speleem-microscope.html.

[8] T. Schmidt, A. Sala, H. Marchetto, E. Umbach, H.-J. Freund, First experimental proof for aberration correction in XPEEM: resolution, transmission enhancement, and limitation by space charge effects, Ultramicrosc 126 (2013) 23–32, https://doi.org/10.1016/j.ultramic.2012.11.004.

[9] M. Patt, C. Wiemann, N. Weber, M. Escher, A. Gloskovskii, W. Drube, M. Merkel, C. M. Schneider, Bulk sensitive hard x-ray photoemission electron microscopy, Rev. Sci. Instrum. 85 (2014) 113704.

[10] B. Schönhense, K. Medjanik, O. Fedchenko, S. Chernov, M. Ellguth, D. Vasilyev, A. Oelsner, J. Viefhaus, D. Kutnyakhov, W. Wurth, H.J. Elmers, G. Schönhense, Multidimensional photoemission spectroscopy – the space-charge limit, New J. Phy. 20 (2018) 033004, https://doi.org/10.1088/1367-2630/aaa262.

[11] D. Kutnyakhov, P. Xian, M. Dendzik, M. Heber, F. Pressacco, S.Y. Agustsson, L. Wenthaus, H. Meyer, S. Gieschen, G. Mercurio, A. Benz, K. Bühlman, S. Däster, R. Gort, D. Curcio, K. Volckaert, M. Bianchi, Ch. Sanders, J.A. Miwa, S. Ulstrup, A. Oelsner, C. Tusche, Y.J. Chen, D. Vasilyev, K. Medjanik, G. Brenner, S. Dziarzhytski, H. Redlin, B. Manschwetus, S. Dong, J. Hauer, L. Rettig, F. Diekmann, K. Rossnagel, J. Demsar, H.J. Elmers, P. Hofmann, R. Ernstorfer, G. Schönhense, Y. Acremann, W. Wurth, Time- and momentum-resolved photoemission studies using time-of-flight momentum microscopy at a free-electron laser, Rev. Sci. Instrum. 91 (2020) 013109, https://doi.org/10.1063/1.5118777.

[12] G.L. Dakovski, M.-F. Lin, D.S. Damiani, W.F. Schlotter, J.J. Turner, D. Nordlund, H. Ogasawara, A novel method for resonant inelastic soft x-ray scattering via photoelectron spectroscopy detection, J. Synchrotron. Radiat. 24 (2017) 1180, https://doi.org/10.1107/S1600577517011869.

[13] O. Tkach, S. Fragkos, Q. Nguyen, S. Chernov, M. Scholz, N. Wind, S. Babenkov, O. Fedchenko, Y. Lytvynenko, D. Zimmer, A. Hloskovskii, D. Kutnyakhov, F. Pressacco, J. Dilling, L. Bruckmeier, M. Heber, F. Scholz, J. A. Sobota, J. D. Koralek, N. Sirica, M. Hoesch, C. Schlueter, L.V. Odnodvorets, Y. Mairesse, K. Rossnagel, H.-J. Elmers, S. Beaulieu and G. Schönhense, *Multi-mode front lens for momentum microscopy: experiments*, e-print on arXiv 2401.10084v2 (2024).

[14] C. Tusche, A. Krasyuk, J. Kirschner, Spin resolved bandstructure imaging with a high resolution momentum microscope, Ultramicrosc 159 (2015) 520, https://doi.org/10.1016/j.ultramic.2015.03.020.

[15] A. Tamai, W. Meevasana, P.D.C. King, C.W. Nicholson, A. de la Torre, E. Rozbicki, F. Baumberger, Spin-orbit splitting of the Shockley surface state on Cu(111), Phys. Rev. B 87 (2013) 075113.

[16] K. Medjanik, O. Fedchenko, S. Chernov, D. Kutnyakhov, M. Ellguth, A. Oelsner, B. Schönhense, T.R.F. Peixoto, P. Lutz, C.-H. Min, F. Reinert, S. Däster, Y. Acremann, J. Viefhaus, W. Wurth, H.J. Elmers, G. Schönhense, Direct 3D mapping of the fermi surface and fermi velocity, Nat Mater 16 (2017) 615, https://doi.org/10.1038/nmat4875.

[17] K. Medjanik, S.V. Babenkov, S. Chernov, D. Vasilyev, B. Schönhense, C. Schlueter, A. Gloskowskii, Yu. Matveyev, W. Drube, H.J. Elmers, G. Schönhense, Progress in HAXPES performance combining full-field k-imaging with time-of-flight recording, J. Synchr. Radiat. 26 (2019) 1996–2012, https://doi.org/10.1107/S1600577519012773.

[18] O. Fedchenko, A. Winkelmann, K. Medjanik, S. Babenkov, D. Vasilyev, S. Chernov, C. Schlueter, A. Gloskovskii, Yu. Matveyev, W. Drube, B. Schönhense, H.J. Elmers, G. Schönhense, High-resolution hard-X-ray photoelectron diffraction in a momentum microscope - the model case of graphite, N. J. Phys. 21 (2019) 113031, https://doi.org/10.1088/1367-2630/ab51fe.

[19] O. Fedchenko, A. Winkelmann, G. Schönhense, Structure analysis using time-of-flight momentum microscopy with hard X-rays: status and prospects, J. Phys. Soc. Jpn. 91 (2022) 091006, https://doi.org/10.7566/JPSJ.91.091006 special volume "Hyper-Ordered Structures".

[20] G. Schönhense, K. Medjanik, O. Fedchenko, A. Zymakova, S. Chernov, D. Kutnyakhov, D. Vasilyev, S. Babenkov, H.J. Elmers, P. Baumgärtel, P. Goslawski, G. Öhrwall, T. Grunske, T. Kauerhof, K. von Volkmann, M. Kallmayer, M. Ellguth, A. Oelsner, Time-of-flight photoelectron momentum microscopy with 80–500 MHz photon sources: electron-optical pulse picker or bandpass pre-filter, J. Synchr. Radiat. 28 (2021) 1891–1908, https://doi.org/10.1107/s1600577521010511.

[21] G. Schönhense, S. Babenkov, D. Vasilyev, H.-J. Elmers, K. Medjanik, Single-hemisphere photoelectron momentum microscope with time-of-flight recording, Rev. Sci. Instrum. 91 (2020) 123110, https://doi.org/10.1063/5.0024074.

[22] C. Tusche, Y.J. Chen, C.M. Schneider, J. Kirschner, Imaging properties of hemispherical electrostatic energy analyzers for high resolution momentum microscopy, Ultramicrosc 206 (2019) 112815, https://doi.org/10.1016/j.ultramic.2019.112815.

[23] G. Schönhense, H. Spiecker, Correction of chromatic and spherical aberrations in electron microscopy utilizing the time-structure of pulsed excitation sources, J. Vac. Sci. Technol. 20 (2002) 2526–2534, https://doi.org/10.1116/1.1523373. B.

[24] R. M. Tromp, J. B. Hannon, W. Wan, A. Berghaus and O. Schaff, *A new aberration-corrected, energy-filtered LEEM/PEEM instrument. II. Operation and results*, ultramicrosc. 127, 25-39 (2013); doi: 10.1016/j.ultramic.2012.07.016.

[25] D.A. Dahl, T.R. McJunkin, J.R. Scott, Comparison of ion trajectories in vacuum and viscous environments using SIMION: insights for instrument design, Int. J. Mass Spectrom. 266 (2007) 156–165. http://www.sisweb.com. primary author: David J. Manura, SIS (version 8.1/8.0/SL).

[26] G. Schönhense and B. Schönhense, *Reduction of space-charge interaction in electron-spectroscopic instruments*, German Patent, DE 10 2017 126 882.0 (filed Nov. 2017).

[27] S. Fragkos, Q. Courtade, O. Tkach, B. Fabre, J. Gaudin, D. Descamps, G. Barrette, S. Petit, G. Schönhense, Y. Mairesse and S. Beaulieu, *Time- and polarization-resolved extreme ultraviolet momentum microscopy*, under review.

[28] S. Fragkos, E. Symeonidou, E. Lasserre, B. Fabre, D. Descamps, S. Petit, P. Tsipas, Y. Mairesse, A. Dimoulas, S. Beaulieu, Excited states band mapping and ultrafast nonequilibrium dynamics in topological dirac semimetal 1T-$ZrTe_2$, Nano Lett., 24 (2024) 13397–13404, https://doi.org/10.1021/acs.nanolett. 4c04019.

[29] S. Fragkos, B. Fabre, O. Tkach, S. Petit, D. Descamps, G. Schönhense, Y. Mairesse, M. Schüler and S. Beaulieu, *Floquet-Bloch Valleytronics*, under review, e-print on arXiv 2412.03935 (2024).

[30] O. Fedchenko, J. Minár, A. Akashdeep, S.W. D'Souza, D. Vasilyev, O. Tkach, L. Odenbreit, Q.L. Nguyen, D. Kutnyakhov, N. Wind, L. Wenthaus, M. Scholz, K. Rossnagel, M. Hoesch, M. Aeschlimann, B. Stadtmüller, M. Kläui, G. Schönhense, T. Jungwirth, A. Birk Hellenes, G. Jakob, L. Smejkal, J. Sinova, H.J. Elmers, Observation of time-reversal symmetry breaking in the band structure of altermagnetic RuO_2, Sci. Adv. 10 (2024) eadj4883, https://doi.org/10.1126/sciadv.adj4883.

[31] H.J. Elmers, O. Tkach, Y. Lytvynenko, P. Yogi, M. Schmitt, D. Biswas, J. Liu, S. V. Chernov, Q.L. Nguyen, M. Hoesch, D. Kutnyakhov, N. Wind, L. Wenthaus, M. Scholz, K. Rossnagel, A. Gloskovskii, C. Schlueter, A. Winkelmann, A.-A. Haghighirad, T.-L. Lee, M. Sing, R. Claessen, M. Le Tacon, J. Demsar, G. Schönhense, O. Fedchenko, Chirality in the Kagome metal CsV_3Sb_5, Phys. Rev. Lett. 134 (2025) 096401, https://doi.org/10.1103/PhysRevLett.134.096401.

[32] F. Pressacco, D. Sangalli, V. Uhlír, D. Kutnyakhov, J. Ander Arregi, S.Y. Agustsson, G. Brenner, H. Redlin, M. Heber, D. Vasilyev, J. Demsar, G. Schönhense, M. Gatti, A. Marini, W. Wurth, F. Sirotti, Subpicosecond metamagnetic phase transition in FeRh driven by non-equilibrium electron dynamics, Nat. Commun. 12 (2021) 5088, https://doi.org/10.1038/s41467-021-25347-3.

[33] V. Shokeen, M. Heber, D. Kutnyakhov, X. Wang, A. Yaroslavtsev, P. Maldonado, M. Berritta, N. Wind, L. Wenthaus, F. Pressacco, C.-H. Min, M. Nissen, S.K. Mahatha, S. Dziarzhytski, P.M. Oppeneer, K. Rossnagel, H.-J. Elmers, G. Schönhense, H. A. Dürr, Real-time observation of phonon-electron energy flow in laser-heated Nickel, Sci. Adv. 10 (2024) eadj2407, https://doi.org/10.1126/sciadv.adj2407.

[34] M. Dendzik, R.P. Xian, E. Perfetto, D. Sangalli, D. Kutnyakhov, S. Dong, S. Beaulieu, T. Pincelli, F. Pressacco, D. Curcio, S.Y. Agustsson, M. Heber, J. Hauer, W. Wurth, G. Brenner, Y. Acremann, P. Hofmann, M. Wolf, A. Marini, G. Stefanucci, L. Rettig, R. Ernstorfer, Observation of an excitonic mott transition through ultrafast core-cum-conduction photoemission spectroscopy, Phys. Rev. Lett. 125 (2020) 096401, https://doi.org/10.1103/PhysRevLett.125.096401.

[35] O. Karni, I. Esin, K.M. Dani, Through the lens of a momentum microscope: viewing light-induced quantum phenomena in two-dimensional materials, Adv. Mater. 35 (2023) 2204120, https://doi.org/10.1002/adma.202204120.

[36] M. Reutzel, G.S.M. Jansen, S. Mathias, Probing excitons with time-resolved momentum microscopy, Adv. Phys. X 9 (2024) 2378722, https://doi.org/10.1080/23746149.2024. 2378722.

[37] R. Wallauer, M. Raths, K. Stallberg, L. Münster, D. Brandstetter, X. Yang, J. Güdde, P. Puschnig, S. Soubatch, C. Kumpf, F.C. Bocquet, F.S. Tautz, U. Höfer, Tracing orbital images on ultrafast time scales, Science 371 (2021) 1056, https://doi.org/10.1126/science.abf3286.

[38] A. Kunin, S. Chernov, J. Bakalis, Z. Li, S. Cheng, Z.H. Withers, M.G. White, G. Schönhense, X. Du, R.K. Kawakami, T.K. Allison, Momentum-resolved intervalley and intravalley exciton coupling in Monolayer WS_2, Phys. Rev. Lett. 130 (2023) 046202, https://doi.org/10.1103/PhysRevLett.130.046202.

[39] G. Schönhense, D. Kutnyakhov, F. Pressacco, M. Heber, N. Wind, S.Y. Agustsson, S. Babenkov, D. Vasilyev, O. Fedchenko, S. Chernov, L. Rettig, B. Schönhense, L. Wenthaus, G. Brenner, S. Dziarzhytski, S. Palutke, S.K. Mahatha, N. Schirmel, H. Redlin, B. Manschwetus, I. Hartl, Yu. Matveyev, A. Gloskovskii, C. Schlueter, V. Shokeen, H. Duerr, T.K. Allison, M. Beye, K. Rossnagel, H.J. Elmers, K. Medjanik, Suppression of the vacuum space-charge effect in fs-photoemission by a retarding electrostatic front lens, Rev. Sci. Instrum. 92 (2021) 053703, https://doi.org/10.1063/5.0046567.

[40] S. Hellmann, C. Sohrt, M. Beye, T. Rohwer, F. Sorgenfrei, M. Marczynski-Bühlow, M. Kalläne, H. Redlin, F. Hennies, M. Bauer, A. Föhlisch, L. Kipp, W. Wurth, K. Rossnagel, Time-resolved x-ray photoelectron spectroscopy at FLASH, N. J. Phys. 14 (2012) 013062, https://doi.org/10.1088/1367-2630/14/1/013062.

[41] L.-P. Oloff, M. Oura, K. Rossnagel, A. Chainani, M. Matsunami, R. Eguchi, T. Kiss, Y. Nakatani, T. Yamaguchi, J. Miyawaki, M. Taguchi, K. Yamagami, T. Togashi, T. Katayama, K. Ogawa, M. Yabashi, T. Ishikawa, Time-resolved HAXPES at

SACLA: probe and pump pulse-induced space-charge effects, N. J. Phys. 16 (2014) 123045, https://doi.org/10.1088/1367-2630/16/12/123045.

[42] X.J. Zhou, B. Wannberg, W.L. Yang, V. Brouet, Z. Sun, J.F. Douglas, D. Dessau, Z. Hussain, Z.-X. Shen, Space charge effect and mirror charge effect in photoemission spectroscopy, J. Electron. Spectrosc. Relat. Phenom. 142 (2005) 27, https://doi.org/10.1016/j.elspec.2004.08.004.

[43] G. Schönhense, K. Medjanik, C. Tusche, M. de Loos, B. van der Geer, M. Scholz, F. Hieke, N. Gerken, J. Kirschner, W. Wurth, Correction of the deterministic part of space-charge interaction in momentum microscopy of charged particles, Ultramicr 159 (2015) 499, https://doi.org/10.1016/j.ultramic.2015.05.015.

[44] T.K. Allison, A. Kunin, G. Schönhense, Cavity-enhanced high-order harmonic generation for high-performance time-resolved photoemission experiments, APL Photon. 10 (2025) 010906, https://doi.org/10.1063/5.0244045.

[45] O. Fedchenko, L. Smejkal, M. Kallmayer, Ya. Lytvynenko, K. Medjanik, S. Babenkov, D. Vasilyev, M. Kläui, J. Demsar, G. Schönhense, M. Jourdan, J. Sinova, H.-J. Elmers, Direct observation of antiferromagnetic parity violation in the electronic structure of Mn_2Au, J. Phys. Condensed Matter 34 (2022) 425501, https://doi.org/10.1088/1361648X/ac87e6.

[46] B.P. Tonner, Energy-filtered imaging with electrostatic optics for photoelectron microscopy, Nucl. Instr. Meth. A 291 (1990) 60, https://doi.org/10.1016/0168-9002(90)90034-4.

[47] E. Bauer, C. Koziol, G. Lilienkamp, T. Schmidt, Spectromicroscopy in a low energy electron microscope, J. Electron. Spectrosc. Relat. Phenom. 84 (1997) 201–209, https://doi.org/10.1016/S0368-2048(97)00007-8.

[48] P. Bernhard, J. Maul, U. Ott, Ch. Sudek, M. Escher, N. Weber, M. Merkel, B. Krömker, D. Funnemann, G. Schönhense, Trace element analysis in presolar stardust grains via full-field XPS-imaging (NanoESCA), Nucl. Instr. Methods B 246 (2006) 275, https://doi.org/10.1016/j.nimb.2005.12.059.

[49] C. Wiemann, M. Patt, S. Cramm, M. Escher, M. Merkel, A. Gloskovskii, S. Thiess, W. Drube, C.M. Schneider, Probing buried layers by photoelectron spectromicroscopy with hard x-ray excitation, Appl. Phys. Lett. 100 (2012) 223106, https://doi.org/10.1063/1.4722940.

[50] H. Seiler, Secondary electron emission in the scanning electron microscope, J. Appl. Phys. 54 (1983) R1–R18, https://doi.org/10.1063/1.332840.

[51] Q.L. Nguyen, J. Simoni, O. Fedchenko, S. Chernov, A. Mishra, Z. Zhang, L. Hoang, O. Tkach, F. Scholz, M. Scholz, K. Rossnagel, D. Ratner, M. Hoesch, N. Sirica, E. Pop, A. Mannix, H.-J. Elmers, G. Schönhense, Spectral imaging of 2D magnetic semiconductor V-WS_2using ToF-XPEEM, LEEMPEEM 13 (2024). Montrealbook of abstracts no. 164, and to be published.

[52] A. Bostwick, MicroARPES and nanoARPES at diffraction limited light sources: opportunities and performance gains, in: E. Rotenberg (Ed.), MicroARPES and nanoARPES at diffraction limited light sources: opportunities and performance gains, J. Synchrotron. Radiat. 21 (2014) 1048–1056, see also A. Bostwick, R.J. Koch and E. Rotenberg, https://sites.google.com/a/lbl.gov/maestro/instrumentation/nanoarpes.

[53] G. Feraco, O. De Luca, P. Przybysz, H. Jafari, O. Zheliuk, Y. Wang, P. Schädlich, P. Dudin, J. Avila, J. Ye, T. Seyller, P. Dabrowski, P.J. Kowalczyk, J. Sławinska, P. Rudolf, A. Grubišic-Cabo, Nano-ARPES investigation of structural relaxation in small angle twisted bilayer tungsten disulfide, Phys. Rev. Mater. 8 (2024) 124004, https://doi.org/10.1103/PhysRevMaterials.8.124004.

[54] S. Chernov et al., publication in preparation.

[55] P. Risterucci, O. Renault, C. Zborowski, D. Bertrand, A. Torres, J.-P. Rueff, D. Ceolin, G. Grenet, S. Tougaard, Effective inelastic scattering cross-sections for background analysis in HAXPES of deeply buried layers, Appl. Surf. Sci. 402 (2017) 78–85, https://doi.org/10.1016/j.apsusc.2017.01.046.

[56] V.N. Strocov, L.L. Lev, M. Kobayashi, C. Cancellieri, M.-A. Husanu, A. Chikina, N.B. M. Schröter, X. Wang, J.A. Krieger, Z. Salman, k-resolved electronic structure of buried heterostructure and impurity systems by soft-X-ray ARPES, J. Electron. Spectrosc. Relat. Phenom. 236 (2019) 1, https://doi.org/10.1016/j.elspec.2019.06.009.

[57] J.O. Schunck, J. Buck, R.Y. Engel, S.R. Kruse, S. Marotzke, M. Scholz, S. K. Mahatha, M.-J. Huang, H.M. Rønnow, G. Dakovski, M. Hoesch, M. Kalläne, K. Rossnagel, M. Beye, A compact approach to higher-resolution resonant inelastic x-ray scattering detection using photoelectrons, New J. Phys. 26 (2024) 053008, https://doi.org/10.1088/1367-2630/ad4206.

[58] G.F. Rempfer, K. Nadakavukaren, O.H. Griffith, Topographical effects in emission microscopy, Ultramicr 5 (1980) 437, https://doi.org/10.1016/0304-3991(80)90044-3.

[59] S.A. Nepijko, N.N. Sedov, G. Schönhense, M. Escher, Xinhe Bao, Weixin Huang, Resolution deterioration in emission electron microscopy due to object roughness, Ann. Phys. 9 (2000) 441, https://doi.org/10.1002/andp.20005120602.

[60] P. Hawkes, E. Kasper, Principles of Electron Optics, 2nd ed., 2, Elsevier, 2018 https://doi.org/10.1016/c2015-0-06653-9.

[61] O. Scherzer, Über einige Fehler von Elektronenlinsen, Z. Physik 101 (1936) 593–603, https://doi.org/10.1007/bf01349606.

[62] H. Rose, Allgemeine Abbildungseigenschaften unrunder Elektronenlinsen mit gerader Achse, Optik (Stuttg) 24 (1967), 36 and 108.